International Journal of
Molecular Sciences

MDPI

Article

Electrochemical Behavior of Reduced Graphene Oxide Supported Germanium Oxide, Germanium Nitride, and Germanium Phosphide as Lithium-Ion Battery Anodes Obtained from Highly Soluble Germanium Oxide

Alexey A. Mikhaylov [1], Alexander G. Medvedev [1], Dmitry A. Grishanov [2], Timur M. Fazliev [1], Vasilii Chernyshev [1], Elena A. Mel'nik [1], Tatiana A. Tripol'skaya [1], Ovadia Lev [2,3] and Petr V. Prikhodchenko [1,*]

[1] Kurnakov Institute of General and Inorganic Chemistry, Russian Academy of Sciences, Leninskii prosp. 31, 119991 Moscow, Russia
[2] The Casali Center of Applied Chemistry, The Institute of Chemistry, The Hebrew University of Jerusalem, Jerusalem 9190401, Israel
[3] The Harvey M. Krueger Family Center for Nanoscience and Nanotechnology, The Hebrew University of Jerusalem, Edmond J. Safra Campus, Jerusalem 9190401, Israel
* Correspondence: prikhman@gmail.com

Abstract: Germanium and germanium-based compounds are widely used in microelectronics, optics, solar cells, and sensors. Recently, germanium and its oxides, nitrides, and phosphides have been studied as active electrode materials in lithium- and sodium-ion battery anodes. Herein, the newly introduced highly soluble germanium oxide (HSGO) was used as a versatile precursor for germanium-based functional materials. In the first stage, a germanium-dioxide-reduced graphene oxide (rGO) composite was obtained by complete precipitation of GeO_2 nanoparticles on the GO from an aqueous solution of HSGO and subsequent thermal treatment in argon at low temperature. The composition of the composite, GeO_2-rGO (20 to 80 wt.% of crystalline phase), was able to be accurately determined by the HSGO to GO ratio in the initial solution since complete deposition and precipitation were achieved. The chemical activity of germanium dioxide nanoparticles deposited on reduced graphene oxide was shown by conversion to rGO-supported germanium nitride and phosphide phases. The GeP-rGO and Ge_3N_4-rGO composites with different morphologies were prepared in this study for the first time. As a test case, composite materials with different loadings of GeO_2, GeP, and Ge_3N_4 were evaluated as lithium-ion battery anodes. Reversible conversion–alloying was demonstrated in all cases, and for the low-germanium loading range (20 wt.%), almost theoretical charge capacity based on the germanium content was attained at 100 mA g^{-1} (i.e., 2595 vs. 2465 mAh g^{-1} for Ge_3N_4 and 1790 vs. 1850 mAh g^{-1} for GeP). The germanium oxide was less efficiently exploited due to its lower conversion reversibility.

Keywords: germanium dioxide; germanium nitride; germanium phosphide; highly soluble germanium oxide; graphene oxide; coating; anode material; lithium-ion battery

Citation: Mikhaylov, A.A.; Medvedev, A.G.; Grishanov, D.A.; Fazliev, T.M.; Chernyshev, V.; Mel'nik, E.A.; Tripol'skaya, T.A.; Lev, O.; Prikhodchenko, P.V. Electrochemical Behavior of Reduced Graphene Oxide Supported Germanium Oxide, Germanium Nitride, and Germanium Phosphide as Lithium-Ion Battery Anodes Obtained from Highly Soluble Germanium Oxide. *Int. J. Mol. Sci.* **2023**, *24*, 6860. https://doi.org/10.3390/ijms24076860

Academic Editor: Jun Wang

Received: 13 March 2023
Revised: 3 April 2023
Accepted: 4 April 2023
Published: 6 April 2023

1. Introduction

Germanium and binary inorganic germanium compounds (GeO_2, GeP, Ge_3N_4) are widely used in various fields of science and technology [1]. Germanium is a critically important semiconductor for microelectronics, optics, solar cells, and sensing. The applications of germanium dioxide are determined by its optical and electrical properties [2] and are characterized by a wide band gap (more than 5 eV), high transparency in the visible and infrared regions, and a high refractive index (1.6–1.7) [3,4]. Germanium phosphide has emerged as an attractive candidate for broad-band and mid-infrared photonics [5]. Germanium nitride has attracted interest due to its unique properties [6–8]. It can be used as

a thin film material for the passivation of semiconductors [9,10], for plasmonic devices [1], and as an effective non-oxide photocatalyst for water splitting [11]. Germanium has higher electrical and ionic conductivity than silicon, which makes it an attractive alternative for high-performance anode material [12–14]. Despite its high cost, elemental germanium and its compounds are promising electrode materials in metal-ion batteries [15–18] due to the large theoretical gravimetric and volumetric specific capacities of germanium (with the formation of $Li_{15}Ge_4$), equal to 1384 mAh g^{-1} and 7366 mAh cm^{-3}, respectively. Unfortunately, large volume changes (by more than 300%) during Li alloying/de-alloying lead to the pulverization of electrode particles and destabilization of solid electrolyte interphase (SEI) films, which hinders the use of germanium-based materials in LIBs [19,20]. Various approaches have been proposed to prevent a dramatic capacitance decrease in Ge-based anodes. For example, the synthesis of carbon-containing composites [21–24], which endow elasticity and conductive network, can significantly increase the long-cycling stability of the anode material. In addition, fabricating nanosized particles or particles of a tailored morphology [20,25,26] is an effective strategy to avoid degradation during cycling. Nowadays, different germanium compounds and their composites are studied as active materials for electrodes of lithium-ion batteries: GeO_2 [27–29], Ge_3N_4, GeP of different stoichiometry [30–36], and germanium chalcogenides (sulfides, selenides, tellurides) [37–39].

Germanium phosphide, which combines the benefits of both germanium and phosphorus, is considered a potential anode for lithium- and sodium-ion batteries. Currently, the main approaches to synthesizing nanosized germanium phosphide are limited to ball milling and separation of GeP particles. The ball milling leads to the formation of irregularly shaped particles with a large size spread (from several tens of nanometers to several microns) [40]. Meanwhile, exfoliated GeP showed relatively low capacity and cyclic stability [35]. Microspheres of germanium phosphide prepared by a solvothermal method showed attractive electrochemical properties as a potential anode material, such as a high first-cycle Coulombic efficiency of 83% and high reversible capacity (1400 mAh g^{-1} after 150 cycles at 0.2 C) [41]. Germanium phosphide particles were obtained by red phosphorus evaporation–condensation on the germanium substrate. The authors demonstrated that the morphology was determined by the morphology of the initial germanium reactant [42].

Compared to the phosphide and oxide, germanium nitride has been less studied as an LIB anode material, perhaps since the first publication showed that only 40% of the material participates in the reaction with lithium ions, and unreacted Ge_3N_4 remains in the core. Therefore, it was concluded that the conversion reaction forming Li_3N is irreversible [43].

Germanium nitride is usually obtained by nitridation with gaseous ammonia at high temperatures and a long annealing time [11,44]. Kim et al. described a new technique for obtaining the Ge_3N_4@C composite by partial oxidation of germanium and nitridation by gaseous NH_3 at 700 °C for 1 h. Subsequent carbonization with acetylene at 800 °C results in Ge_3N_4@C powder with a specific capacity of 600–700 mAh g^{-1} at 550 mA g^{-1} for 300 cycles as a LIB anode [45].

The introduction of carbon components, such as graphene or carbon nanotubes, can enhance the performance of the germanium oxide LIB anode. The observed reversible capacity was close to or even higher than the theoretical reversible capacity of germanium oxide [23,26,29,46–50]. These observations show the possible partial reversibility of Li_2O formation. Lv et al. calculated that 44.4–44.6% of Li_2O matrix participates in the reverse alloying during cycling at 100 mA g^{-1} due to intimate contact between graphene layers and GeO_x nanoparticles [51]. However, the significant irreversible capacity loss of the first cycle remains a severe problem for germanium oxide anode materials [52].

We have previously reported on the green-hydrogen-peroxide-assisted sol–gel processing route to deposit thin films of p-block peroxo compounds on various substrates [53,54]. The thermal or chemical treatment of these coatings on graphene oxide layers results in the formation of the corresponding oxides, sulfides, and tellurides, which are effective as lithium-, sodium-, and potassium-ion battery anodes [50,55–65]. In particular, a peroxogermanate thin film was deposited in high yield at room temperature on graphene

oxide from peroxogermanate sols [50]. Thermal treatment of the filtered material produced amorphous germanium dioxide, crystalline germanium dioxide, and elemental germanium films supported by reduced graphene oxide (rGO). The obtained composites exhibited high cycling stability and good rate performance as LIB anodes.

The germanium compounds are expensive reagents, which calls for processing protocols with a quantitative yield of germanium. For this, there is a need for new convenient starting germanium compounds with higher reactivity and better water solubility compared to known precursors. Herein, we report an environmentally friendly method for the preparation of germanium-based composite materials from a highly soluble germanium oxide (HSGO) and the performance of the Ge composite products as anode materials in lithium-ion batteries. Germanium phosphide and nitride were selected as target materials for two reasons: (i) The high lithium conductivities of lithium nitride and phosphide—the lithiation by-products of GeP and Ge_3N_4. Lithium nitride and lithium phosphide are known lithium superconductors [66,67], and amorphous Li_3N [68,69] and Li_3P [67,70] were also reported to exhibit high ionic conductivity (10^{-3} S·cm^{-1}). (ii) To improve the performance of germanium compounds as LIB anodes, it is, of course, essential to exhibit high Ge-Li alloying performance, but the performance can be further enhanced by exploiting the charge capacity of the conversion reaction associated with the counter element. Due to the lower electronegativity of nitrogen and phosphorous compared to oxygen, the respective bond cleavage and reversibility of the reactions of lithium phosphide and nitride should be better than Li_2O.

2. Results and Discussion

2.1. Synthesis

The choice of an effective germanium precursor in the form of a highly soluble form of amorphous germanium oxide made it possible accurately dose the amount of germanium introduced into the system and opened new possibilities for controlling the morphology and composition of composite materials. HSGO was obtained by rapid decomposition of ammonium peroxogermanate $(NH_4)_6[Ge_6(\mu\text{-}OO)_6(\mu\text{-}O)_6(OH)_6].6H_2O$ at 300 °C [71]. We have already demonstrated that HSGO has a high solubility (up to 100 g per liter of water) and reactivity and, therefore, is a convenient starting reagent for the preparation of various germanium compounds [71,72]. However, until now, HSGO has not been used to obtain germanium-based composite functional materials or electrode materials. The first stage of synthesis was the deposition of a film of germanium oxide nanoparticles on the surface of graphene oxide sheets from an aqueous solution of HSGO. High solubility of precursors in water allows for easy regulation of the loading of germanium dioxide in obtained materials. Three different loadings of germanium dioxide were chosen for subsequent thermal and chemical processing, namely, 20, 50, and 80 wt.% of GeO_2. The addition of aqueous ammonia to the solution of HSGO increased the pH from 5.5 to about 8. Precipitation of germanium oxide species on the graphene oxide was then accomplished by the addition of ethanol, resulting in uniform amorphous germanium-based coating (Figure S1). According to X-ray powder diffractometry, the crystalline phase of germanium dioxide was not formed even for the highest loading of germanium (Figure 1a). Subsequent heat treatment at a relatively low temperature of 300 °C for 3 h resulted in the reduction of graphene oxide and the crystallization of nanosized germanium dioxide. The XRD of the product revealed broad low-intensity peaks that were assigned to the GeO_2 phase (PDF 01-073-9108) (Figure 1c). After the heat treatment, the coating morphology did not contain large agglomerates on the rGO surface and retained the morphology of the initial material (Figures 2a,b and S1).

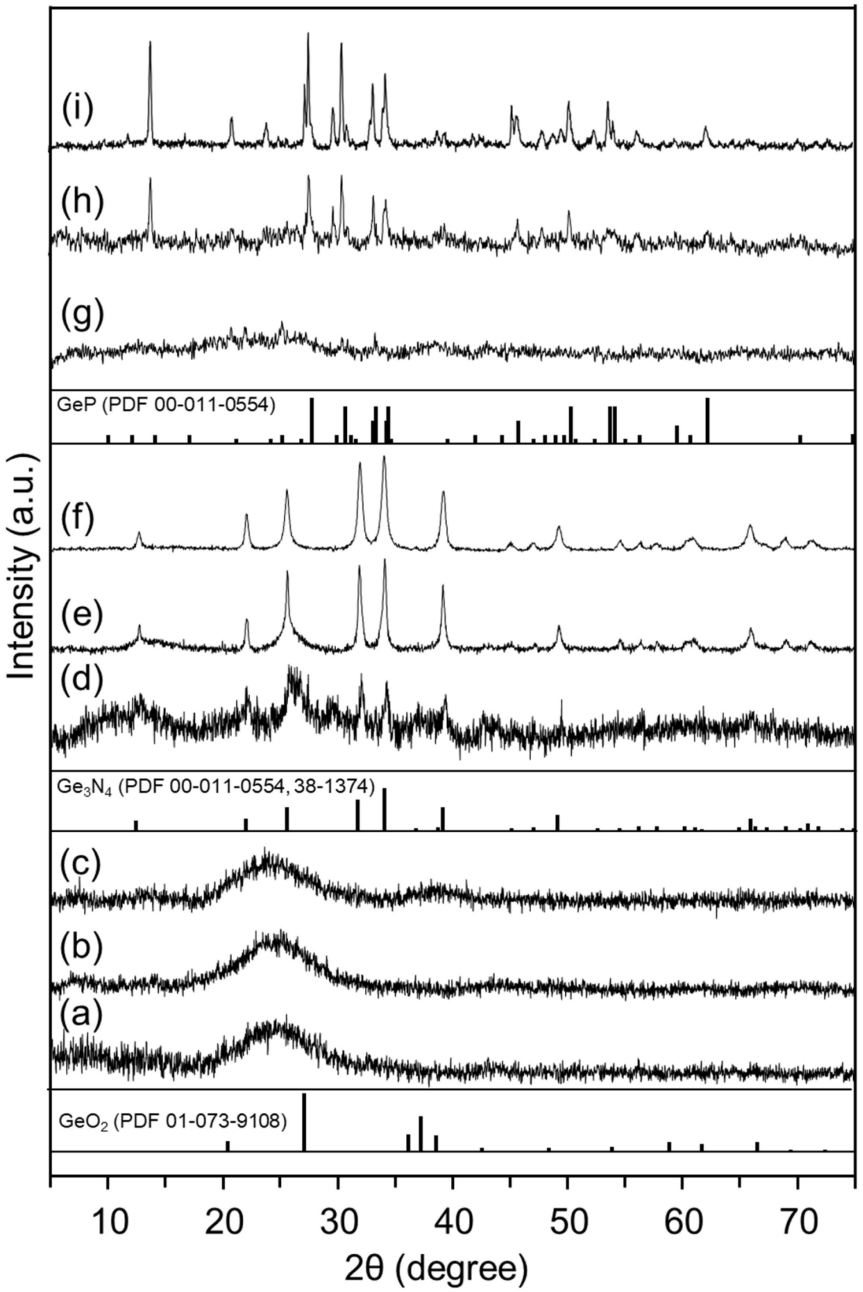

Figure 1. Powder X-ray diffractograms of GeO_2-rGO-20 (**a**), GeO_2-rGO-50 (**b**), GeO_2-rGO-80 (**c**), Ge_3N_4-rGO-20 (**d**), Ge_3N_4-rGO-50 (**e**), Ge_3N_4-rGO-80 (**f**), GeP-rGO-20 (**g**), GeP-rGO-50 (**h**), and GeP-rGO-80 (**i**) powders. Vertical bars below represent the standard diffraction data for corresponding crystalline germanium compounds.

According to the CHN analysis, the amount of carbon in GeO_2-rGO composites corresponded to the initial ratio of HSGO to GO, resulting in 16.7, 42.9, and 75.5 wt.% for 20, 50, and 80 wt.% of GO, respectively. The reduction of graphene oxide, accompanied by the removal of oxygen-containing functional groups, decreased the carbon content in the heated materials, GeO_2-rGO (Table 1). The CHN confirms the high yield of composite material in terms of germanium. Thus, the described procedure was a simple, low-cost, and highly effective method for the preparation of GeO_2-rGO composite.

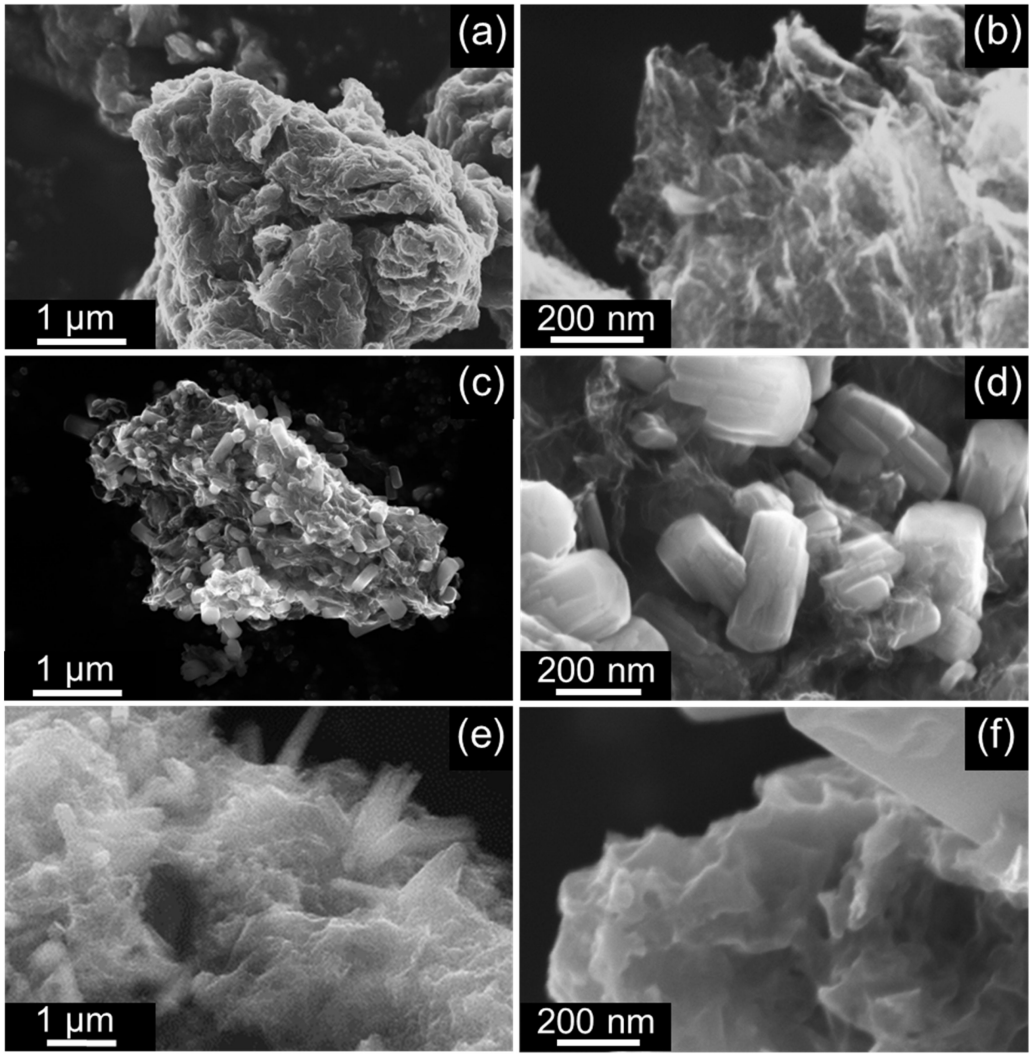

Figure 2. SEM images of GeO_2-rGO-80 (**a**,**b**), Ge_3N_4-rGO-80 (**c**,**d**), and GeP-rGO-80 (**e**,**f**).

Table 1. Elemental analysis of GeO_2-rGO, Ge_3N_4-rGO, and GeP-rGO materials.

Material	C, wt.% (by CHN)	N, wt.% (by CHN)	Ge:P, at:at (by EDX)
GeO_2-rGO-80	16.7		
GeO_2-rGO-50	42.9		
GeO_2-rGO-20	75.5		
Ge_3N_4-rGO-80	25.0	12.0	
Ge_3N_4-rGO-50	48.0	9.4	
Ge_3N_4-rGO-20	76.2	6.8	
GeP-rGO-80	13.5		1.1
GeP-rGO-50	45.1		0.9
GeP-rGO-20	74.3		1.2

The GeO_2-rGO composites are used as a suitable initial material for preparing crystalline germanium nitride and phosphide-decorated rGO. As far as we know, this is the first attempt to obtain rGO-supported Ge_3N_4 and GeP composites. Previously, only the corresponding carbonized phases were obtained and characterized [34,45]. The lack of research can be attributed to the limited number of wet methods for obtaining germanium oxide–graphene oxide composites due to the low solubility of germanium oxide.

Prolonged treatment of GeO_2-rGO-80 by gaseous NH_3 at 700 °C for 2 h yields long wires of germanium nitride (Figure S2). Reduced treatment time (up to 5–10 min) results in

Ge_3N_4 agglomerates with an average size of 50–200 nm, which decorate the rGO surface (Figure 2c,d). It should be noted that a part of the crystalline phase appears as a uniform coating on the surface of reduced graphene oxide (Figure S3). An attempt to control the particle size of germanium nitride was made by adjusting the ratio between the loading of germanium dioxide and graphene oxide. Decreasing of GeO_2 loading to 20 wt.% (GeO_2-rGO-20) resulted in a uniform coating of Ge_3N_4 crystalline phase, as shown by the SEM and EDX analyses (Figure S4). Treatment of GeO_2-rGO-50 by ammonia formed a Ge_3N_4-rGO-50 composite consisting of rGO decorated with about 100 nm nitride particles. EDX mapping (Figure S5) showed that a thin layer of the Ge_3N_4 phase uniformly coated the rGO surface. We were able to estimate the mass content of the germanium nitride phase on the basis of the CHN analysis. The calculated loadings of germanium nitride were 58.7, 45.7, and 33.5 wt.% for Ge_3N_4-rGO-80, Ge_3N_4-rGO-50, and Ge_3N_4-rGO-20, respectively (Table 1). The calculated values indicated the presence of a residual germanium dioxide phase in the Ge_3N_4-rGO-80 sample. The powder diffractograms of Ge_3N_4-rGO samples reflected the structure of β-Ge_3N_4 (PDF 00-011-0554, Figure 1d–f). Both samples contained an admixture of a low-crystallinity phase of germanium nitride that appeared as a background and broad peaks according to the corresponding diffractograms. Thus, the Ge_3N_4-rGO-50 and Ge_3N_4-rGO-80 were refined (by the methodology in reference [73] as composites with bimodal crystallite size distributions. The average crystallite size for the germanium nitride phase, which appeared as a uniform coating, was around 2 nm in all three samples, while the anchored particles were characterized by 20.5 and 31.5 nm in Ge_3N_4-rGO-50 and Ge_3N_4-rGO-80, respectively. The large particle parameters were able to be significantly affected by crystallite shape.

Heat treatment of GeO_2-rGO material with red phosphorus in a sealed quartz tube led to the formation of a germanium phosphide phase, which was clearly confirmed by X-ray powder diffraction data (Figure 1g–i). The scanning electron microscopy and energy-dispersive X-ray spectroscopy demonstrated the formation of both a uniform coating of germanium phosphide on the surface of reduced graphene oxide and relatively large particles of germanium phosphide with an average crystallite size of 168 nm (computed by the Scherrer equation), as in the case of germanium nitride with a high loading of germanium dioxide in the starting material (Figures 2e,f and S6). Similar to the synthetic procedure of germanium nitride, the decrease in the content of GeO_2 to 50% formed particles with a smaller crystallite size of 38.4 nm. Subsequent decreasing of GeO_2 loading to 20% revealed a uniform coating of reduced graphene oxide by germanium phosphide with an average crystallite size of 2.2 nm (Figures S7 and S8), similar to values obtained by Rietveld refinement of experimental data for materials with higher Ge loading. According to the EDX analysis, the Ge/P ratio corresponded to the GeP crystalline phase (Table 1).

Using HSGO as a precursor allowed us to, firstly, accurately control the amount of active material loaded into the system and, secondly, to form a uniform coating of germanium oxide on graphene oxide. In addition, regulating the germanium oxide-graphene oxide ratio and the reaction time allowed for the obtaining of materials of different morphologies. Thus, highly soluble germanium oxide is a suitable and effective precursor for fabricating germanium-based materials of various compositions and morphologies, which was demonstrated by synthesizing germanium nitride and phosphide composites of reduced graphene oxide. As a test case, all nine obtained composites were evaluated as active materials of anodes in lithium-ion batteries to demonstrate the usefulness, uniqueness, and versatility of the HSGO-based synthesis approach.

2.2. Electrochemical Evaluation

Cyclic voltammetry was carried out to determine the electrochemical properties of the composites at room temperature. The CV plot of GeO_2-rGO-80 is shown in Figure 3a. The first reduction scan shows a shallow shoulder at 1.07, which was previously attributed to minor lithiation of the germanium oxide to form Li_yGeO_2. An intensive peak at 0.4 V was attributed to the formation of the SEI layer overlapping a conversion reaction (Li_yGeO_2

to Ge(0)). Then, a cathodic wave, at E < 0.2 V, was attributed to a Ge-Li alloying process: ($xLi + Ge \rightarrow Li_xGe$ ($0 \leq x \leq 4.4$)). Similarly, the discharge peaks on subsequent cycles at about 0.98 V and 0.46 V vs. Li/Li^+ and the cathodic wave at <0.2 V were attributed to minute alloying to form Li_yGeO_2, a conversion reaction that produced elemental Ge and then Ge-Li alloying [24,50]. The charging peaks were present at 0.44 and 1.14 V. The first related to dealloying, and the second indicated the (re)oxidation of Ge to GeO_2 [50,51,74].

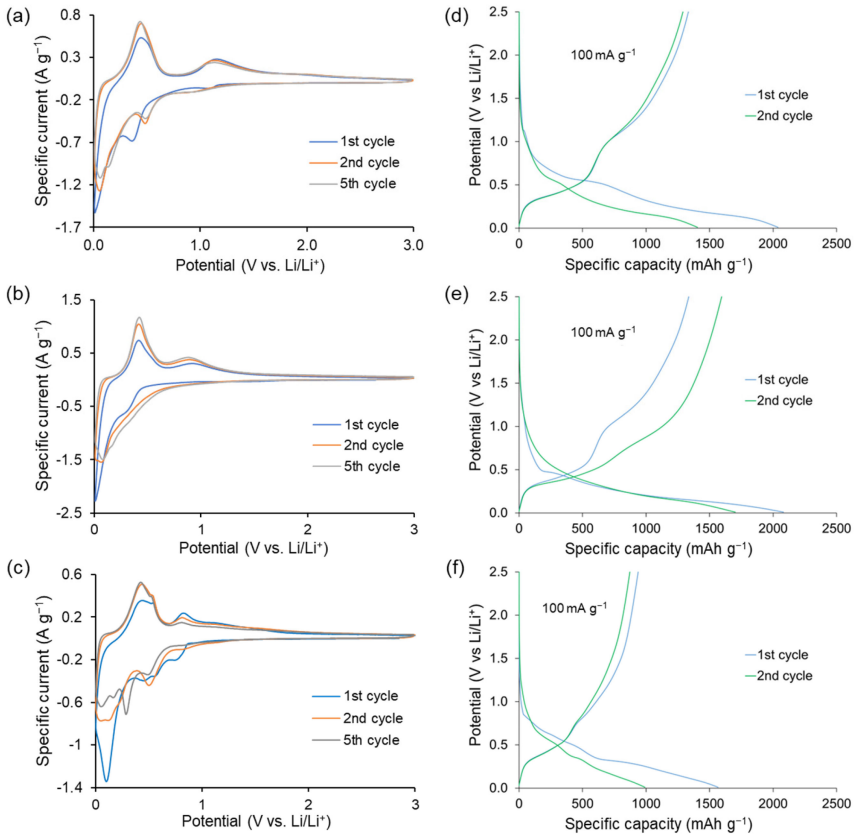

Figure 3. Cycling voltammetry of GeO_2-rGO-80 (**a**), Ge_3N_4-rGO-80 (**b**), and GeP-rGO-80 (**c**) at 0.1 mV s^{-1}. First and second charge−discharge curves for GeO_2-rGO-80 (**d**), Ge_3N_4-rGO-80 (**e**), and GeP-rGO-80 (**f**) at 100 mA g^{-1}.

The CV plot of the Ge_3N_4-rGO-80 anode was similar to the GeO_2-rGO electrode (Figure 3b) and reflected the alloying–conversion reactions. As indicated by Pereira et al. [43], there is practically only one reduction wave corresponding to the conversion and alloying reaction (Equation (1)).

$$Ge_3N_4 + 3(4 + x)Li^+ + 3(4 + x)e^- \rightarrow 3Li_xGe + 4Li_3N, \quad (1)$$

where $0 \leq x \leq 4.4$. Pereira et al. [43] attributed the overlap of the alloying and conversion waves to the rapid reductive alloying of Ge(0) to form Li_xGe alloy phases. The small shoulder, at 0.2 V, on the first discharging scan may also be attributed to this alloying reaction. The two anodic peaks at 0.4 and 0.9 V were attributed to the delithiation reaction ($Li_xGe \rightarrow Ge + xLi^+ + xe^-$) and the partial recovery of lithium germanium nitride Li_zGe_yN, although full recovery of the original germanium nitride Ge_3N_4 was unable to be proven by X-ray, and Pereira et al. [43] did not identify this phase. The persistence of the 0.9 V anodic peak (Figure 3b) showed that the conversion reaction was partially reversible, and nitride (re)formation contributed significantly to the observed charge capacity. The same can be concluded on the basis of the relatively moderate (around 18%) capacity loss in the first cycle. Irreversible formation of the inactive Li_3N phase was noted [45], and Periera et al. [43] even reported that the 0.9 V peak disappeared after long cycling. Therefore, we

carried out cyclic voltammetry of the Ge_3N_4-rGO-80 electrode after 150 discharge–charge cycles at 100 mA g^{-1} (Figure S10). The figure clearly indicates the presence of the 0.9 V peak and confirms the capacity contribution of reversible Li_3N formation even after long cycling. The intimate contact between the germanium nitride coating and graphene oxide could be responsible for the favorable reversibility of the germanium nitride conversion reaction in this study. The CV plots of GeO_2-rGO-20 and Ge_3N_4-rGO-20 are presented in Figure S9. They indicate the validity of our conclusions regarding the lower potential at which the conversion of germanium nitride took place compared to germanium oxide and the higher contribution of the conversion reaction in the former.

Figure 3c depicts the CV plots of the germanium phosphide anode, GeP-rGO-80. The study was conducted under the same conditions used to investigate the germanium oxide and germanium nitride electrodes. Comparison of the CV plots with the literature allows us to assign the following processes [30,32,35,40]. The interval 1.0–0.68 V corresponded to lithium intercalation with the formation of the Li_xGeP phase. The subsequent stage of conversion with the formation of Li_3P and Ge appeared as peaks in the range of 0.68–0.40 V. The 0.4–0.005 V peaks were assigned to the alloying stage with Li_yGe formation. At the charging scan, the active electrode demonstrated electrochemical oxidation peaks at the 0.005–0.68 V interval assigned to the Li_yGe dealloying process. The next potential window at 0.68–1.1 V was attributed to the reversal of the conversion reaction with Li_xGeP formation. The broad, low-intensity peak at higher potentials was assigned to the deintercalation reaction, which led to the GeP formation. The lower germanium phosphide loading (GeP-rGO-20) provided a similar CV plot (Figure S9c) but with much lower currents and less distinct peaks. The germanium phosphide anodes, similar to the germanium nitride electrodes, exhibited significant reversibility and charge contribution to the conversion reaction. However, in all cases, the alloying reactions contributed a much larger charge capacity than the conversion reactions.

The galvanostatic charge–discharge curves of the three different germanium compounds are presented in Figure 3d–f. The first and second cycles at 100 mA g^{-1} showed good first cycle efficiency of about 68, 80, and 63% for GeO_2-rGO-80, Ge_3N_4-rGO-80, and GeP-rGO-80, respectively, which were not inferior and mostly exceeded the best-published values, including those tested at a narrower potential window of up to 1.5 V [33,43,45,50].

The specific capacities depended on the Ge content in the active phase loadings (Figure 4). We carried out long cycling stability tests for 150 cycles at 100 mA g^{-1} and evaluated the rate performance at 100–3000 mA g^{-1} at a potential window of 0.005–3.0 V vs. Li/Li^+. The decreases in specific capacity after 150 charge–discharge cycles compared to the second cycle were 44% (from 1404 to 785 mAh g^{-1}), 66% (from 1696 to 575 mAh g^{-1}), and 58% (from 990 to 408 mAh g^{-1}) for the GeO_2-rGO-80, Ge_3N_4-rGO-80, and GeP-rGO-80 anodes, respectively. The obtained results were not inferior to the recently reported data for GeO_2 [23,24,50], Ge_3N_4 [43,45], and GeP anodes [35]. This can be attributed to the large volume expansion of the inorganic phase.

The electrode materials with lower germanium content demonstrated good cycling stability for germanium oxide, nitride, and phosphide. The specific cycling capacities of the Ge_3N_4-rGO-20 and GeP-rGO-20 were higher than for GeO_2-rGO-80 after long cycling at 100 mA g^{-1}. The capacity drops after 150 cycles were only 17% (from 714 to 592 mA g^{-1}) and 23% (from 610 to 468 mA g^{-1}) for Ge_3N_4-rGO-20 and GeP-rGO-20, respectively, while for GeO_2-rGO-20 material, it was 51% (from 710 to 345 mA g^{-1}). The increased stability at low loading can be attributed to the higher physical buffering of the larger fraction of the (flexible) rGO or to the better adhesion of the small nanoparticles to the rGO surface, having a larger specific contact area with the rGO support (i.e., contact area to the rGO per crystallite weight). Support for the second explanation was indirectly provided by the performance of the GeO_2 electrodes, which exhibited monomodal particle size distribution (even for the 80 wt.% GeO_2 loading) but exhibited similar cyclic stabilities at different germanium loadings.

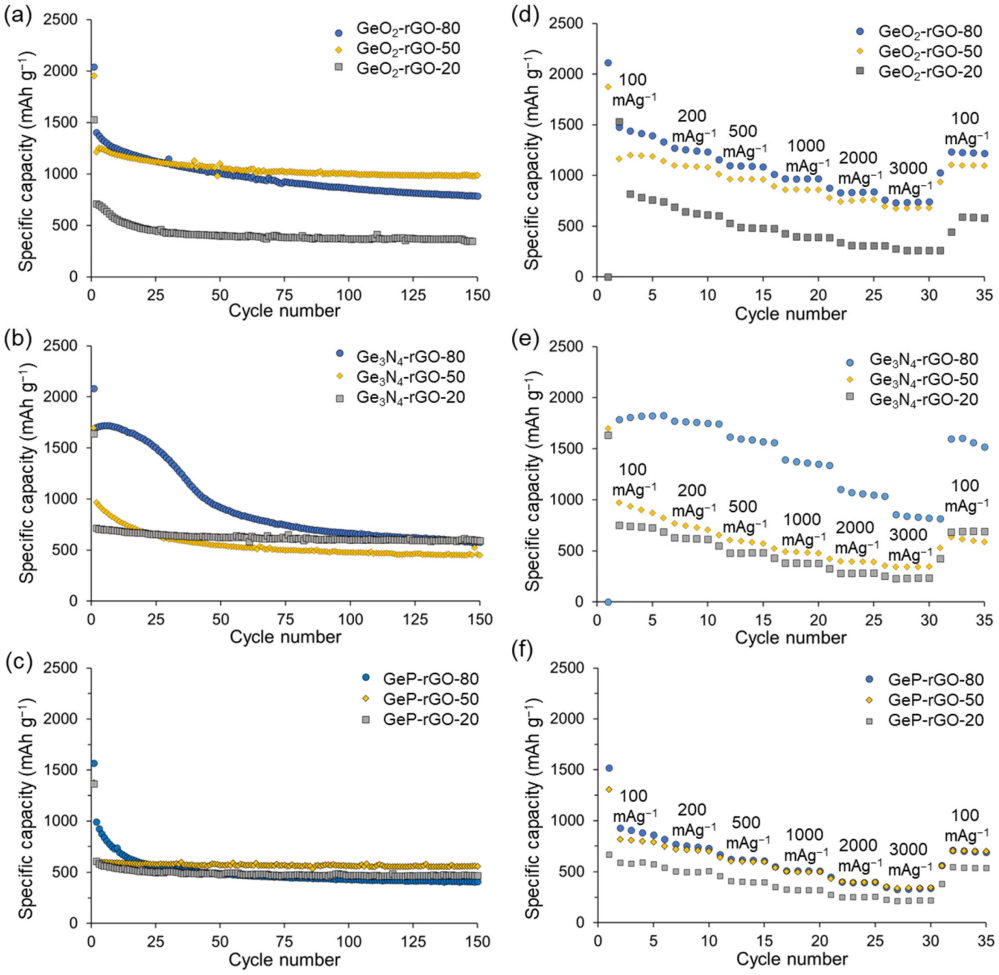

Figure 4. Cycling voltammetry of GeO_2-rGO-80 (**a**), Ge_3N_4-rGO-80 (**b**), and GeP-rGO-80 (**c**) at 0.1 mV s^{-1}. First and second charge−discharge curves for GeO_2-rGO-80 (**d**), Ge_3N_4-rGO-80 (**e**), and GeP-rGO-80 (**f**) at 100 mA g^{-1}.

According to CHN analysis, the carbon content in Ge_3N_4-rGO-20 and GeP-rGO-20 samples were equal to 76.2 and 74.2 wt.%, respectively (Table 1), corresponding to the ≈24 and ≈26 wt.% content of germanium nitride and phosphide, respectively. Thus, the approximate specific capacity values per gram of Ge_3N_4 and GeP were equal to 2595 and 1790 mAh g^{-1} at a 100 mAg^{-1} scan rate, respectively. The obtained values were close to the theoretical capacity for Ge_3N_4 (2465 mAh g^{-1}) and GeP (1850 mAh g^{-1}) charge capacities, indicating highly efficient Ge_3N_4-rGO-20 and GeP-rGO-20 electrode materials and the reversibility of Li_3N matrix formation. In this argument, we ignored the contribution of the graphene oxide to the capacity, which, at most, would amount to 280 mA per g of active germanium compound. Comparison of a CV plot for a germanium nitride anode with higher and lower loadings of active phase (Figure 3b and Figure S9b, respectively) with those for germanium oxide allowed us to conclude with regards to the reversible Li_3N formation resulting in higher specific capacity of germanium nitride electrodes.

The rate capabilities of germanium dioxide, nitride, and phosphide composite anodes with different loading of reduced graphene oxide at 100 to 3000 mA g^{-1} currents are presented in Figure 4d–f, respectively. All materials demonstrated good high-rate performance. An increase in charge–discharge current by a factor of 30 to 3000 mA g^{-1} resulted in the preservation of 33, 36, and 46% of the specific charge capacity of Ge_3N_4-rGO-20, Ge_3N_4-rGO-50, and Ge_3N_4-rGO-80 materials, respectively (Figure 4e). The GeP-based materials retained around 40% of the initial capacity at a high rate of 3000 mA g^{-1} (Figure 4f). Similar values, equal to 32, 50, and 48%, were obtained for initial germanium dioxide–rGO

composites with 20, 50, and 80% loading of the inorganic phase, respectively. To the best of our knowledge, the obtained specific capacity value of 830 mAh g^{-1} at 3000 mA g^{-1} for Ge_3N_4-rGO-80 is the highest attained for electrodes based on germanium nitride, while the experimental values for germanium oxide and phosphide are similar to the best-published values [35].

We tested the GeO_2-rGO-80, Ge_3N_4-rGO-80, and GeP-rGO-80 materials for cycling stability at a high rate of 1000 mA g^{-1} (Figure S11). The specific capacity values were equal to 360, 390, and 300 mAh g^{-1} after 500 cycles for GeO_2-rGO-80, Ge_3N_4-rGO-80, and GeP-rGO-80, respectively.

Conversion anodes are characterized by high-voltage hysteresis and, thus, poorer energy efficiency compared to alloying and conversion-alloying anodes [75–79]. Since the electrodes exhibited considerable conversion reaction contribution, the voltage hysteresis was computed. The calculation protocol is provided in the Supporting Information. The average voltage hystereses calculated at the 30th cycle at 100 mA g^{-1} were equal to 0.70, 0.46, and 0.51 V for GeO_2-rGO-80, Ge_3N_4-rGO-80, and GeP-rGO-80, respectively. The germanium nitride and phosphide anodes exhibited lower voltage hystereses compared to the GeO_2-rGO anode and to other conversion electrodes, and their voltage hystereses were similar to tin sulfide electrodes, which exhibited a voltage hysteresis of 0.48 V [79]. The comparison of the voltage hysteresis, $\overline{\Delta V}$ of several conversion LIB anodes, was reported by Zhong et al. [80]. The best voltage hystereses of LIB anodes, namely, Fe_3O_4 and MnO, showed $(\overline{\Delta V}) > 0.55$ V, which was higher than the values obtained for the germanium nitride LIB anode. This was not surprising. The Ge-based anodes studied in this research were better classified as conversion–alloying anodes rather than conversion reaction electrodes.

3. Materials and Methods

3.1. Synthetic Procedures

3.1.1. Synthesis of Highly Soluble Germanium Oxide (HSGO)

Synthesis was conducted according to [71]. Briefly, 0.5208 g of $GeCl_4$ (2.43 mmol) was added to 20 mL of 5 wt.% H_2O_2. The precipitate was dispersed in an ultrasonic bath for 2 min. The dispersion was neutralized with 2 mL of NH_4OH (12.5 wt.% solution) until pH 9. After an additional 5 min of stirring, 20 mL of alcohol was added for full precipitation. The precipitate was separated by filtration on a glass filter and washed three times with 3 mL of 50 wt.% EtOH, once with 3 mL EtOH, and once with 3 mL diethyl ether. A total of 0.3892 g of APG was obtained after drying (92.2% yield based on Ge). Then, 0.389 g of APG was heated in a furnace at 300 °C for 15 min to produce 0.231 g of HSGO powder (98.7% yield based on Ge).

3.1.2. Preparation of Graphene Oxide (GO) Dispersion

GO was synthesized from exfoliated graphite by a modified Hummers method, and a detailed protocol is described in our previous articles [54,58,64].

3.1.3. Synthesis of GeO_2-rGO

A total of 7.5 g of aqueous GO dispersion (1.2 wt.%) was mixed with 17.5 mL of DIW with sonication. Then, 350 mg of HSGO and 1 mL of NH_4OH 25 wt.% aqueous solution were introduced. The precipitation of GeO_2 onto the GO surface was accomplished by the addition of 100 mL of ethanol under vigorous stirring. The coated GO was centrifuged and washed two times with ethanol and once with diethyl ether. The material was dried under vacuum at room temperature and then heated in Ar at 300 °C for 3 h. Samples with different GeO_2 loading were prepared and assigned as GeO_2-rGO-80, GeO_2-rGO-50, and GeO_2-rGO-20.

3.1.4. Synthesis of Ge_3N_4-rGO

GeO_2-rGO powders with different Ge loading were introduced to the hot tube furnace under dry NH_3 flow at 700 °C for 10 min. Dark powder was obtained and assigned as Ge_3N_4-rGO-80, Ge_3N_4-rGO-50, and Ge_3N_4-rGO-20.

3.1.5. Synthesis of GeP-rGO

The GeO_2-rGO materials were mixed with red phosphorous and sealed in a quartz tube. The tube was heated at 590 °C for 2 h. Dark gray powder was collected and assigned as GeP-rGO-80, GeP-rGO-50, and GeP-rGO-20 depending on the initial GeO_2 loading.

3.2. Material Characterization

Details of the material characterization techniques are provided in the Supplementary Information.

3.3. Electrochemical Measurements

The active electrode material was mixed with Super P (Alfa Aesar) and polyvinylidene difluoride (PVDF) (Sigma-Aldrich) in a weight ratio of 70:15:15 with N-methyl pyrrolidone (NMP) as the medium to form a slurry. The slurry was then coated on a roughened copper foil as a current collector using a doctor blade. The electrode was then dried at 80 °C and pressed in a roll press. The electrodes were cut into 16 mm diameter discs and further dried at 110 °C for 4 h in a vacuum before being introduced into an argon-filled glovebox. The average loading of active material on the Cu foil was 1.5–2 mg cm^{-2}. The electrodes were assembled with Li metal counter electrodes in a 2016-type coin cell. A total of 1 M $LiPF_6$ in EC:DEC was used as an electrolyte. Then, 5% v/v fluorinated ethylene carbonate (FEC, Alfa Aesar) was added to the electrolyte to improve solid electrolyte interface (SEI) stability. The coin cells were assembled in an Ar-filled glovebox with less than 0.1 ppm oxygen. The charge/discharge tests were performed with a Neware battery tester within a voltage window of 0.01–3.0 V vs. Li/Li^+ at 100–3000 mA g^{-1} rate. Cyclic voltammetry (0.005–3.0 V, 0.1 mV s^{-1}) was performed with a VersaSTAT3 potentiostat.

4. Conclusions

As far as we know, this is the first report on the Ge_3N_4-rGO and GeP-rGO composites. The highly soluble germanium oxide (HSGO) was used as a versatile precursor of germanium-based electrode materials. HSGO was prepared in mild conditions with high yield from the germanium coordination peroxo compound, namely, ammonium peroxogermanate (APG), $(NH_4)_6[Ge_6(\mu\text{-}OO)_6(\mu\text{-}O)_6(OH)_6]\cdot 6H_2O$. In the first stage, HSGO was used as a precursor for the deposition of uniform coating consisting of germanium dioxide nanoparticles on reduced graphene oxide (GeO_2-rGO). The loading of GeO_2 phase was regulated by the ratio of HSGO and graphene oxide starting materials since full conversion was demonstrated. The highly reactive germanium dioxide on graphene oxide support allows for the conversion of the oxide to nitride and phosphide phases. It was shown that the morphology of Ge_3N_4 and GeP crystalline phases depended on the loading of germanium dioxide in the GeO_2-rGO composite. For low loadings of 20 wt.% germanium compound, only a very thin film of active material was obtained, whereas at higher loading, coatings with bimodal size distribution were demonstrated.

The homogeneous distribution of germanium compounds (exclusively) over the surface of the graphene oxide was demonstrated in all the electrode coatings. However, in the germanium phosphide and nitride electrodes, the particle size distribution was bimodal, comprised of approximately 2 nm thick homogenous coverage of the rGO surface and larger nanoparticles of around 200 nm particles densely decorating the surface. The ratio between these two phases was a function of the germanium oxide loading; only thin-film coating was formed from 20 wt.% GeO_2 loading, while the fraction of the large particles was considerably higher for the materials prepared from the 80 wt.% GeO_2 loading. The charge capacity was accordingly higher for the high-loading materials, but alloying pulver-

ization was much lower for the active materials with smaller particles. Excellent stability of Ge_3N_4-rGO-20 and GeP-rGO-20 composites was demonstrated by 150 cycles at 100 mA g^{-1} with charge capacity loss of less than 17% and 23%, respectively, in the last 150 cycles. The higher stability of the low Ge-loaded anodes was attributed to the superior adhesion of the uniform nanoparticle coverage of the rGO and its larger specific contact area rather than to the higher carbon content, since GeO_2 electrodes did not exhibit superior stability at low germanium loading.

Germanium is an expensive resource, and therefore, even for niche applications, its theoretical charge capacity should be approached. The Ge_3N_4-rGO-20 and GeP-rGO-20 demonstrate that even at a 100 mA g^{-1} rate, the conversion reaction was close to quantitative, and the almost theoretical charge capacity of the germanium compounds was approached: 2595 vs. 2465 mAh g^{-1} for Ge_3N_4 and 1790 vs. 1850 mAh g^{-1} for GeP. The germanium oxide was less efficiently exploited due to its lower conversion reversibility compared to GeP and Ge_3N_4 electrodes, following previous reports.

Supplementary Materials: The following supporting information can be downloaded at https://www.mdpi.com/article/10.3390/ijms24076860/s1.

Author Contributions: Conceptualization, A.G.M., P.V.P. and O.L.; methodology, A.G.M. and P.V.P.; synthesis, D.A.G., A.A.M., T.M.F., V.C., E.A.M. and T.A.T.; characterization, A.A.M., A.G.M., D.A.G., E.A.M. and T.A.T.; writing—original draft preparation, A.A.M., A.G.M. and P.V.P.; writing—review and editing, O.L.; visualization, A.A.M., A.G.M., T.M.F. and E.A.M.; supervision, P.V.P.; project administration, A.G.M., P.V.P. and O.L.; funding acquisition, A.G.M. All authors have read and agreed to the published version of the manuscript.

Funding: This research was funded by Russian Science Foundation, grant number 23-23-00583, https://rscf.ru/en/project/23-23-00583/ (accessed on 3 April 2023).

Institutional Review Board Statement: Not applicable.

Informed Consent Statement: Not applicable.

Data Availability Statement: The data presented in this study are available in the article and Supplementary Materials.

Acknowledgments: This work was conducted using the experimental facilities of the JRC PMR IGIC RAS.

Conflicts of Interest: The authors declare no conflict of interest.

References

1. Emsley, J. *Nature's Building Blocks: Everything You Need to Know about the Elements*; Oxford University Press: Oxford, UK, 2011.
2. Lange, T.; Njoroge, W.; Weis, H.; Beckers, M.; Wuttig, M. Physical Properties of Thin GeO_2 Films Produced by Reactive DC Magnetron Sputtering. *Thin Solid Films* **2000**, *365*, 82–89. [CrossRef]
3. Xu, M.-F.; Shi, X.-B.; Jin, Z.-M.; Zu, F.-S.; Liu, Y.; Zhang, L.; Wang, Z.-K.; Liao, L.-S. Aqueous Solution-Processed GeO_2: An Anode Interfacial Layer for High Performance and Air-Stable Organic Solar Cells. *ACS Appl. Mater. Interfaces* **2013**, *5*, 10866–10873. [CrossRef] [PubMed]
4. Wang, Z.K.; Li, M.; Yuan, D.X.; Shi, X.B.; Ma, H.; Liao, L.S. Improved Hole Interfacial Layer for Planar Perovskite Solar Cells with Efficiency Exceeding 15%. *ACS Appl. Mater. Interfaces* **2015**, *7*, 9645–9651. [CrossRef] [PubMed]
5. Wang, Z.; Guo, J.; Zhang, Y.; Liu, J.; Ponraj, J.S.; Dhanabalan, S.C.; Zhai, T.; Liu, X.; Song, Y.; Zhang, H. 2D GeP-Based Photonic Device for near-Infrared and Mid-Infrared Ultrafast Photonics. *Nanophotonics* **2020**, *9*, 3645–3654. [CrossRef]
6. Hayakawa, R.; Yoshida, M.; Ide, K.; Yamashita, Y.; Yoshikawa, H.; Kobayashi, K.; Kunugi, S.; Uehara, T.; Fujimura, N. Structural Analysis and Electrical Properties of Pure Ge_3N_4 Dielectric Layers Formed by an Atmospheric-Pressure Nitrogen Plasma. *J. Appl. Phys.* **2011**, *110*, 064103. [CrossRef]
7. Yuan, L.; Han, C.; Yang, M.-Q.; Xu, Y.-J. Photocatalytic Water Splitting for Solar Hydrogen Generation: Fundamentals and Recent Advancements. *Int. Rev. Phys. Chem.* **2016**, *35*, 1–36. [CrossRef]
8. Jishiashvili, D.; Kapaklis, V.; Devaux, X.; Politis, C.; Kutelia, E.; Makhatadze, N.; Gobronidze, V.; Shiolashvili, Z. Germanium Nitride Nanowires Produced by Thermal Annealing in Hydrazine Vapor. *Adv. Sci. Lett.* **2009**, *2*, 40–44. [CrossRef]
9. Zhang, S.L.; Wang, W.; Zhang, E.H.; Xiao, W. Half-Metallic Ferromagnetism in Transition-Metal Doped Germanium Nitride: A First-Principles Study. *Phys. Lett. A* **2010**, *374*, 3234–3237. [CrossRef]

10. Yang, M.; Wang, S.J.; Peng, G.W.; Wu, R.Q.; Feng, Y.P. Ab Initio Study on Intrinsic Defect Properties of Germanium Nitride Considered for Gate Dielectric. *Appl. Phys. Lett.* **2007**, *91*, 132906. [CrossRef]
11. Maeda, K.; Saitoh, N.; Inoue, Y.; Domen, K. Dependence of Activity and Stability of Germanium Nitride Powder for Photocatalytic Overall Water Splitting on Structural Properties. *Chem. Mater.* **2007**, *19*, 4092–4097. [CrossRef]
12. Liu, Y.; Zhang, S.; Zhu, T. Germanium-Based Electrode Materials for Lithium-Ion Batteries. *ChemElectroChem* **2014**, *1*, 706–713. [CrossRef]
13. Bogart, T.D.; Chockla, A.M.; Korgel, B.A. High Capacity Lithium Ion Battery Anodes of Silicon and Germanium. *Curr. Opin. Chem. Eng.* **2013**, *2*, 286–293. [CrossRef]
14. Li, X.; Yang, Z.; Fu, Y.; Qiao, L.; Li, D.; Yue, H.; He, D. Germanium Anode with Excellent Lithium Storage Performance in a Germanium/Lithium–Cobalt Oxide Lithium-Ion Battery. *ACS Nano* **2015**, *9*, 1858–1867. [CrossRef]
15. Sierra, L.; Gibaja, C.; Torres, I.; Salagre, E.; Avilés Moreno, J.R.; Michel, E.G.; Ocón, P.; Zamora, F. Alpha-Germanium Nanolayers for High-Performance Li-Ion Batteries. *Nanomaterials* **2022**, *12*, 3760. [CrossRef]
16. Loaiza, L.C.; Monconduit, L.; Seznec, V. Si and Ge-Based Anode Materials for Li-, Na-, and K-Ion Batteries: A Perspective from Structure to Electrochemical Mechanism. *Small* **2020**, *16*, 1905260. [CrossRef]
17. Liang, S.; Cheng, Y.J.; Zhu, J.; Xia, Y.; Müller-Buschbaum, P. A Chronicle Review of Nonsilicon (Sn, Sb, Ge)-Based Lithium/Sodium-Ion Battery Alloying Anodes. *Small Methods* **2020**, *4*, 200218. [CrossRef]
18. Liu, X.; Wu, X.Y.; Chang, B.; Wang, K.X. Recent Progress on Germanium-Based Anodes for Lithium Ion Batteries: Efficient Lithiation Strategies and Mechanisms. *Energy Storage Mater.* **2020**, *30*, 146–169. [CrossRef]
19. Kennedy, T.; Mullane, E.; Geaney, H.; Osiak, M.; O'Dwyer, C.; Ryan, K.M. High-Performance Germanium Nanowire-Based Lithium-Ion Battery Anodes Extending over 1000 Cycles through in Situ Formation of a Continuous Porous Network. *Nano Lett.* **2014**, *14*, 716–723. [CrossRef]
20. Chan, C.K.; Zhang, X.F.; Cui, Y. High Capacity Li Ion Battery Anodes Using Ge Nanowires. *Nano Lett.* **2008**, *8*, 307–309. [CrossRef]
21. Lee, G.-H.; Kwon, S.J.; Park, K.-S.; Kang, J.-G.; Park, J.-G.; Lee, S.; Kim, J.-C.; Shim, H.-W.; Kim, D.-W. Germanium Microflower-on-Nanostem as a High-Performance Lithium Ion Battery Electrode. *Sci. Rep.* **2014**, *4*, 6883. [CrossRef]
22. Li, D.; Feng, C.; Liu, H.K.; Guo, Z. Hollow Carbon Spheres with Encapsulated Germanium as an Anode Material for Lithium Ion Batteries. *J. Mater. Chem. A* **2015**, *3*, 978–981. [CrossRef]
23. Ngo, D.T.; Kalubarme, R.S.; Le, H.T.T.; Park, C.-N.; Park, C.-J. Conducting Additive-Free Amorphous GeO_2/C Composite as a High Capacity and Long-Term Stability Anode for Lithium Ion Batteries. *Nanoscale* **2015**, *7*, 2552–2560. [CrossRef] [PubMed]
24. Koo, J.H.; Paek, S.M. Microwave-Assisted Synthesis of Ge/GeO_2-Reduced Graphene Oxide Nanocomposite with Enhanced Discharge Capacity for Lithium-Ion Batteries. *Nanomaterials* **2021**, *11*, 319. [CrossRef] [PubMed]
25. Liu, J.; Song, K.; Zhu, C.; Chen, C.C.; Van Aken, P.A.; Maier, J.; Yu, Y. Ge/C Nanowires as High-Capacity and Long-Life Anode Materials for Li-Ion Batteries. *ACS Nano* **2014**, *8*, 7051–7059. [CrossRef] [PubMed]
26. Jahel, A.; Darwiche, A.; Matei Ghimbeu, C.; Vix-Guterl, C.; Monconduit, L. High Cycleability Nano-GeO_2/Mesoporous Carbon Composite as Enhanced Energy Storage Anode Material in Li-Ion Batteries. *J. Power Source* **2014**, *269*, 755–759. [CrossRef]
27. McNulty, D.; Geaney, H.; Buckley, D.; O'Dwyer, C. High Capacity Binder-Free Nanocrystalline GeO_2 Inverse Opal Anodes for Li-Ion Batteries with Long Cycle Life and Stable Cell Voltage. *Nano Energy* **2018**, *43*, 11–21. [CrossRef]
28. Yan, S.; Song, H.; Lin, S.; Wu, H.; Shi, Y.; Yao, J. GeO_2 Encapsulated Ge Nanostructure with Enhanced Lithium-Storage Properties. *Adv. Funct. Mater.* **2019**, *29*, 1807946. [CrossRef]
29. Son, Y.; Park, M.; Son, Y.; Lee, J.-S.; Jang, J.-H.; Kim, Y.; Cho, J. Quantum Confinement and Its Related Effects on the Critical Size of GeO_2 Nanoparticles Anodes for Lithium Batteries. *Nano Lett.* **2014**, *14*, 1005–1010. [CrossRef]
30. Li, W.; Li, X.; Yu, J.; Liao, J.; Zhao, B.; Huang, L.; Abdelhafiz, A.; Zhang, H.; Wang, J.H.; Guo, Z.; et al. A Self-Healing Layered GeP Anode for High-Performance Li-Ion Batteries Enabled by Low Formation Energy. *Nano Energy* **2019**, *61*, 594–603. [CrossRef]
31. Kulova, T.L.; Skundin, A.M.; Gavrilin, I.M.; Kudryashova, Y.O.; Martynova, I.K.; Novikova, S.A. Binder-Free Ge-Co-P Anode Material for Lithium-Ion and Sodium-Ion Batteries. *Batteries* **2022**, *8*, 98. [CrossRef]
32. Li, W.; Li, H.; Lu, Z.; Gan, L.; Ke, L.; Zhai, T.; Zhou, H. Layered Phosphorus-like GeP_5: A Promising Anode Candidate with High Initial Coulombic Efficiency and Large Capacity for Lithium Ion Batteries. *Energy Environ. Sci.* **2015**, *8*, 3629–3636. [CrossRef]
33. Li, X.; Li, W.; Shen, P.; Yang, L.; Li, Y.; Shi, Z.; Zhang, H. Layered GeP-Black P(Ge_2P_3): An Advanced Binary-Phase Anode for Li/Na-Storage. *J. Ceram. Int.* **2019**, *45*, 15711–15714. [CrossRef]
34. Yan, Y.; Ruan, J.; Xu, H.; Xu, Y.; Pang, Y.; Yang, J.; Zheng, S. Fast and Stable Batteries with High Capacity Enabled by Germanium-Phosphorus Binary Nanoparticles Embedded in a Porous Carbon Matrix via Metallothermic Reduction. *ACS Appl. Mater. Interfaces* **2020**, *12*, 21579–21585. [CrossRef]
35. Shen, H.; Huang, Y.; Chang, Y.; Hao, R.; Ma, Z.; Wu, K.; Du, P.; Guo, B.; Lyu, Y.; Wang, P.; et al. Narrowing Working Voltage Window to Improve Layered GeP Anode Cycling Performance for Lithium-Ion Batteries. *ACS Appl. Mater. Interfaces* **2020**, *12*, 17466–17473. [CrossRef]
36. Kulova, T.; Gryzlov, D.; Skundin, A.; Gavrilin, I.; Kudryashova, Y.; Pokryshkin, N. Anode Material Synthesized from Red Phosphorus and Germanium Nanowires for Lithium-Ion and Sodium-Ion Batteries. *Int. J. Electrochem. Sci* **2021**, *16*, 211229. [CrossRef]
37. Nam, K.H.; Sung, G.K.; Choi, J.H.; Youn, J.S.; Jeon, K.J.; Park, C.M. New High-Energy-Density GeTe-Based Anodes for Li-Ion Batteries. *J. Mater. Chem. A* **2019**, *7*, 3278–3288. [CrossRef]

38. Wei, Y.; Huang, L.; He, J.; Guo, Y.; Qin, R.; Li, H.; Zhai, T. Healable Structure Triggered by Thermal/Electrochemical Force in Layered $GeSe_2$ for High Performance Li-Ion Batteries. *Adv. Energy Mater.* **2018**, *8*, 1703635. [CrossRef]
39. Feng, D.; Liu, Q.; Li, Z.; Zeng, T. Confining Nano-GeS_2 in Cross-Linked Porous Carbon Networks for High-Performance and Flexible Li-Ion Battery Anodes. *ACS Appl. Energy Mater.* **2021**, *4*, 6096–6105. [CrossRef]
40. Zeng, T.; Feng, D.; Liu, Q.; Hao, S.; Zhou, R. Boosting Cyclability Performance of GeP Anode via In-Situ Generation of Free Expansion Volume. *J. Alloys Compd.* **2021**, *883*, 160857. [CrossRef]
41. Tseng, K.W.; Huang, S.B.; Chang, W.C.; Tuan, H.Y. Synthesis of Mesoporous Germanium Phosphide Microspheres for High-Performance Lithium-Ion and Sodium-Ion Battery Anodes. *Chem. Mater.* **2018**, *30*, 4440–4447. [CrossRef]
42. Kulova, T.; Gryzlov, D.; Skundin, A.; Gavrilin, I.; Martynova, I.; Kudryashova, Y. Causes of Germanium Phosphide Degradation under Prolonged Cycling. *EIS Study. Int. J. Electrochem. Sci.* **2022**, *17*, 220224. [CrossRef]
43. Pereira, N.; Balasubramanian, M.; Dupont, L.; McBreen, J.; Klein, L.C.; Amatucci, G.G. The Electrochemistry of Germanium Nitride with Lithium. *J. Electrochem. Soc.* **2003**, *150*, A1118. [CrossRef]
44. Nakhutsrishvili, I.G.; Dzhishiashvili, D.A.; Miminoshvili, E.B.; Mushkudiani, M.A. Preparation of Germanium Oxynitride Films in Ammonia. *Inorg. Mater.* **2000**, *36*, 1340–1341. [CrossRef]
45. Kim, C.; Hwang, G.; Jung, J.W.; Cho, S.H.; Cheong, J.Y.; Shin, S.; Park, S.; Kim, I.D. Fast, Scalable Synthesis of Micronized Ge_3N_4@C with a High Tap Density for Excellent Lithium Storage. *Adv. Funct. Mater.* **2017**, *27*, 1605975. [CrossRef]
46. Ramana, C.V.; Troitskaia, I.B.; Gromilov, S.A.; Atuchin, V.V. Electrical Properties of Germanium Oxide with α-Quartz Structure Prepared by Chemical Precipitation. *Ceram. Int.* **2012**, *38*, 5251–5255. [CrossRef]
47. Qiu, H.; Zeng, L.; Lan, T.; Ding, X.; Wei, M. In Situ Synthesis of GeO_2/Reduced Graphene Oxide Composite on Ni Foam Substrate as a Binder-Free Anode for High-Capacity Lithium-Ion Batteries. *J. Mater. Chem. A* **2015**, *3*, 1619–1623. [CrossRef]
48. Qin, W.; Chen, T.; Hu, B.; Sun, Z.; Pan, L. GeO_2 Decorated Reduced Graphene Oxide as Anode Material of Sodium Ion Battery. *Electrochim. Acta* **2015**, *173*, 193–199. [CrossRef]
49. Ma, D.-L.; Yuan, S.; Huang, X.-L.; Cao, Z.-Y. Synthesis of Ultrathin GeO_2-Reduced Graphene Oxide (RGO) Sheets for a High-Capacity Lithium-Ion Battery Anode. *Energy Technol.* **2014**, *2*, 342–347. [CrossRef]
50. Medvedev, A.G.; Mikhaylov, A.A.; Grishanov, D.A.; Yu, D.Y.W.; Gun, J.; Sladkevich, S.; Lev, O.; Prikhodchenko, P.V. GeO_2 Thin Film Deposition on Graphene Oxide by the Hydrogen Peroxide Route: Evaluation for Lithium-Ion Battery Anode. *ACS Appl. Mater. Interfaces* **2017**, *9*, 9152–9160. [CrossRef]
51. Lv, D.; Gordin, M.L.; Yi, R.; Xu, T.; Song, J.; Jiang, Y.B.; Choi, D.; Wang, D. GeOx/Reduced Graphene Oxide Composite as an Anode for Li-Ion Batteries: Enhanced Capacity via Reversible Utilization of Li_2O along with Improved Rate Performance. *Adv. Funct. Mater.* **2014**, *24*, 1059–1066. [CrossRef]
52. Qin, J.; Cao, M. Multidimensional Germanium-Based Materials as Anodes for Lithium-Ion Batteries. *Chem.-Asian J.* **2016**, *11*, 1169–1182. [CrossRef]
53. Sladkevich, S.; Mikhaylov, A.A.; Prikhodchenko, P.V.; Tripol'skaya, T.A.; Lev, O. Antimony Tin Oxide (ATO) Nanoparticle Formation from H_2O_2 Solutions: A New Generic Film Coating from Basic Solutions. *Inorg. Chem.* **2010**, *49*, 9110–9112. [CrossRef]
54. Sladkevich, S.; Gun, J.; Prikhodchenko, P.V.; Gutkin, V.; Mikhaylov, A.A.; Medvedev, A.G.; Tripol'skaya, T.A.; Lev, O. The Formation of a Peroxoantimonate Thin Film Coating on Graphene Oxide (GO) and the Influence of the GO on Its Transformation to Antimony Oxides and Elemental Antimony. *Carbon* **2012**, *50*, 5463–5471. [CrossRef]
55. Grishanov, D.A.; Mikhaylov, A.A.; Medvedev, A.G.; Gun, J.; Prikhodchenko, P.V.; Xu, Z.J.; Nagasubramanian, A.; Srinivasan, M.; Lev, O. Graphene Oxide-Supported β-Tin Telluride Composite for Sodium- and Lithium-Ion Battery Anodes. *Energy Technol.* **2018**, *6*, 127–133. [CrossRef]
56. Mikhaylov, A.A.; Medvedev, A.G.; Tripol'skaya, T.A.; Popov, V.S.; Mokrushin, A.S.; Krut'ko, D.P.; Prikhodchenko, P.V.; Lev, O. H_2O_2 Induced Formation of Graded Composition Sodium-Doped Tin Dioxide and Template-Free Synthesis of Yolk–Shell SnO_2 Particles and Their Sensing Application. *Dalton Transact.* **2017**, *46*, 16171–16179. [CrossRef]
57. Mikhaylov, A.A.; Medvedev, A.G.; Grishanov, D.A.; Sladkevich, S.; Gun, J.; Prikhodchenko, P.V.; Xu, Z.J.; Nagasubramanian, A.; Srinivasan, M.; Lev, O. Vanadium Oxide Thin Film Formation on Graphene Oxide by Microexplosive Decomposition of Ammonium Peroxovanadate and Its Application as a Sodium Ion Battery Anode. *Langmuir* **2018**, *34*, 2741–2747. [CrossRef]
58. Prikhodchenko, P.V.; Gun, J.; Sladkevich, S.; Mikhaylov, A.A.; Lev, O.; Tay, Y.Y.; Batabyal, S.K.; Yu, D.Y.W. Conversion of Hydroperoxoantimonate Coated Graphenes to Sb_2S_3 Graphene for a Superior Lithium Battery Anode. *Chem. Mater.* **2012**, *24*, 4750–4757. [CrossRef]
59. Lakshmi, V.; Chen, Y.; Mikhaylov, A.A.; Medvedev, A.G.; Sultana, I.; Rahman, M.M.; Lev, O.; Prikhodchenko, P.V.; Glushenkov, A.M. Nanocrystalline SnS_2 Coated onto Reduced Graphene Oxide: Demonstrating the Feasibility of a Non-Graphitic Anode with Sulfide Chemistry for Potassium-Ion Batteries. *Chem. Commun.* **2017**, *53*, 8272–8275. [CrossRef]
60. Lakshmi, V.; Mikhaylov, A.A.; Medvedev, A.G.; Zhang, C.; Ramireddy, T.; Rahman, M.M.; Cizek, P.; Golberg, D.; Chen, Y.; Lev, O.; et al. Probing Electrochemical Reactivity in an Sb_2S_3-Containing Potassium-Ion Battery Anode: Observation of an Increased Capacity. *J. Mater. Chem. A* **2020**, *8*, 11424–11434. [CrossRef]
61. Prikhodchenko, P.V.; Yu, D.Y.W.; Batabyal, S.K.; Uvarov, V.; Gun, J.; Sladkevich, S.; Mikhaylov, A.A.; Medvedev, A.G.; Lev, O. Nanocrystalline Tin Disulfide Coating of Reduced Graphene Oxide Produced by the Peroxostannate Deposition Route for Sodium Ion Battery Anodes. *J. Mater. Chem. A* **2014**, *2*, 8431–8437. [CrossRef]

62. Mikhaylov, A.A.; Medvedev, A.G.; Mason, C.W.; Nagasubramanian, A.; Madhavi, S.; Batabyal, S.K.; Zhang, Q.; Gun, J.; Prikhodchenko, P.V.; Lev, O. Graphene Oxide Supported Sodium Stannate Lithium Ion Battery Anodes by the Peroxide Route: Low Temperature and No Waste Processing. *J. Mater. Chem. A* **2015**, *3*, 20681–20689. [CrossRef]
63. Yu, D.Y.W.; Batabyal, S.K.; Gun, J.; Sladkevich, S.; Mikhaylov, A.A.; Medvedev, A.G.; Novotortsev, V.M.; Lev, O.; Prikhodchenko, P.V. Antimony and Antimony Oxide@graphene Oxide Obtained by the Peroxide Route as Anodes for Lithium-Ion Batteries. *Main Group Metal Chem.* **2015**, *38*, 43–50. [CrossRef]
64. Sladkevich, S.; Gun, J.; Prikhodchenko, P.V.; Gutkin, V.; Mikhaylov, A.A.; Novotortsev, V.M.; Zhu, J.X.; Yang, D.; Hng, H.H.; Tay, Y.Y.; et al. Peroxide Induced Tin Oxide Coating of Graphene Oxide at Room Temperature and Its Application for Lithium Ion Batteries. *Nanotechnology* **2012**, *23*, 485601. [CrossRef] [PubMed]
65. Yu, D.Y.W.; Prikhodchenko, P.V.; Mason, C.W.; Batabyal, S.K.; Gun, J.; Sladkevich, S.; Medvedev, A.G.; Lev, O. High-Capacity Antimony Sulphide Nanoparticle-Decorated Graphene Composite as Anode for Sodium-Ion Batteries. *Nat. Commun.* **2013**, *4*, 2922. [CrossRef]
66. Alpen, U.V.; Rabenau, A.; Talat, G.H. Ionic Conductivity in Li_3N Single Crystals. *Appl. Phys. Lett.* **2008**, *30*, 621. [CrossRef]
67. Nazri, G. Preparation, Structure and Ionic Conductivity of Lithium Phosphide. *Solid State Ion.* **1989**, *34*, 97–102. [CrossRef]
68. Hayashi, A.; Iio, K.; Morimoto, H.; Minami, T.; Tatsumisago, M. Mechanochemical Synthesis of Amorphous Solid Electrolytes Using SiS_2 and Various Lithium Compounds. *Solid State Ion.* **2004**, *175*, 637–640. [CrossRef]
69. Miyamura, M.; Tomura, S.; Imai, A.; Inomata, S. Electrochemical Studies of Lithium Nitride Solid Electrolyte for Electrochromic Devices. *Solid State Ion.* **1981**, *3–4*, 149–152. [CrossRef]
70. Nazri, G. Preparation, Characterization and Conductivity of Li_3N, Li_3P and Li_3As. *MRS Proc.* **1988**, *135*, 117–130. [CrossRef]
71. Grishanov, D.A.; Churakov, A.V.; Medvedev, A.G.; Mikhaylov, A.A.; Lev, O.; Prikhodchenko, P.V. Crystalline Ammonium Peroxogermanate as a Waste-Free, Fully Recyclable Versatile Precursor for Germanium Compounds. *Inorg. Chem.* **2019**, *58*, 1905–1911. [CrossRef]
72. Kansuzyan, A.V.; Farafonova, S.D.; Saverina, E.A.; Krylova, I.V.; Balycheva, V.A.; Akyeva, A.Y.; Medvedev, A.G.; Nikolaevskaya, E.N.; Egorov, M.P.; Prikhodchenko, P.V.; et al. Highly Soluble Germanium Dioxide as a New Source of Germanium for Derivatization with Organic Compounds. *Mend. Commun.* **2022**, *32*, 25–27. [CrossRef]
73. Uvarov, V.; Popov, I. An Estimation of the Correctness of XRD Results Obtained from the Analysis of Materials with Bimodal Crystallite Size Distribution. *CrystEngComm* **2015**, *17*, 8300–8306. [CrossRef]
74. Wei, W.; Guo, L. One-Step In Situ Synthesis of GeO_2/Graphene Composites Anode for High-Performance Li-Ion Batteries. *Part. Part. Syst. Charact.* **2013**, *30*, 658–661. [CrossRef]
75. Yu, L.; Wang, L.P.; Liao, H.; Wang, J.; Feng, Z.; Lev, O.; Loo, J.S.C.; Sougrati, M.T.; Xu, Z.J. Understanding Fundamentals and Reaction Mechanisms of Electrode Materials for Na-Ion Batteries. *Small* **2018**, *14*, 1703338. [CrossRef]
76. Li, L.; Zheng, Y.; Zhang, S.; Yang, J.; Shao, Z.; Guo, Z. Recent Progress on Sodium Ion Batteries: Potential High-Performance Anodes. *Energy Environ. Sci.* **2018**, *11*, 2310–2340. [CrossRef]
77. Lee, Y.T.; Kuo, C.T.; Yew, T.R. Investigation on the Voltage Hysteresis of Mn_3O_4 for Lithium-Ion Battery Applications. *ACS Appl. Mater. Interfaces* **2021**, *13*, 570–579. [CrossRef]
78. Wang, J.; Wang, L.; Eng, C.; Wang, J. Elucidating the Irreversible Mechanism and Voltage Hysteresis in Conversion Reaction for High-Energy Sodium–Metal Sulfide Batteries. *Adv. Energy Mater.* **2017**, *7*, 1602706. [CrossRef]
79. Mikhaylov, A.A.; Medvedev, A.G.; Buldashov, I.A.; Fazliev, T.M.; Mel'nik, E.A.; Tripol'skaya, T.A.; Sladkevich, S.; Nikolaev, V.A.; Lev, O.; Prikhodchenko, P.V. Green Synthesis of Zinc Sulfide-Reduced Graphene Oxide Composite and Its Application in Sodium-Ion Batteries. *J. Alloys Compd.* **2022**, *910*, 164769. [CrossRef]
80. Zhong, K.; Xia, X.; Zhang, B.; Li, H.; Wang, Z.; Chen, L. MnO Powder as Anode Active Materials for Lithium Ion Batteries. *J. Power Source* **2010**, *195*, 3300–3308. [CrossRef]